Engineering Fracture Mechanics 110 (2013) 81–98

Contents lists available at ScienceDirect

Engineering Fracture Mechanics

journal homepage: www.elsevier.com/locate/engfracmech

Experimental analysis and truss-like discrete element model simulation of concrete specimens under uniaxial compression

I. Iturrioz [a], G. Lacidogna [b,*], A. Carpinteri [b]

[a] Federal University of Rio Grande do Sul, Department of Mechanical Engineering, Porto Alegre, RS, Brazil
[b] Politecnico di Torino, Department of Structural, Geotechnical and Building Engineering, Torino, Italy

ARTICLE INFO

Article history:
Received 6 March 2012
Received in revised form 28 April 2013
Accepted 15 July 2013
Available online 25 July 2013

Keywords:
Concrete
Truss-like discrete element model
Acoustic Emission technique
Gutenberg–Richter law
Damage parameter

ABSTRACT

In this work, the Acoustic Emission signals were captured by sensors applied to the external surfaces of a prismatic concrete specimen subjected to compression loads. In this context, the experimental results are presented in terms of stress–time diagram and also, the variation in the Gutenberg–Richter law, that is, the relation proposed between the Acoustic Emission cumulative counts and its magnitude. This law is obtained during each phase of the test and in the final stage.

A three-dimensional lattice model, known as truss-like Discrete Element Method, also modeled the same specimen. The numerical results present a good correlation with those obtained from the experimental test also in terms of typical Acoustic Emission parameters, such as count rate, cumulative counts, and the variation in the Gutenberg–Richter law.

Using the truss-like discrete element model, the relationship between the Acoustic Emission signal magnitude and the energy released from each localized rupture has also been analyzed. The obtained results are compatible with the Gutenberg–Richter energy–magnitude relation. Finally, the numerical results have been analyzed in terms of Acoustic Emission signal frequency. The simulation presents the same pattern with the experimental results: a shift towards lower Acoustic Emission signal frequencies during the evolution of the damage process.

1. Introduction

From a physical point of view, the phenomenon of damage can be seen as surface discontinuities in the form of cracks, or volume discontinuities in the form of cavities [1,2]. Since the size of cracks or interior defects cannot be identified, it is very difficult to macroscopically distinguish a highly damaged element from an undamaged one. Therefore, it becomes necessary to define internal variables, which are directly accessible to measurement, in order to represent the deteriorated state of the material [1–3].

An advanced method for the quantitative non-destructive evaluation of damage progression is the Acoustic Emission (AE) technique. Physically, AE is a phenomenon caused by the structural alteration of a solid material, in which transient elastic-waves are generated due to a rapid release of strain energy. AEs are also known as stress-wave emissions. AE waves, whose frequencies usually range from kHz to MHz, propagate through the material towards the surface of the structural element, then, sensors, which turn the released strain energy packages into electrical signals [4–13], can detect them. In the present study, USAM resonant sensors (accepting signals from 50 to 800 kHz frequency range) have been used, since concrete strongly attenuates emissions and high sensitivity is required [9,10,13]. Traditionally, in AE testing, a number of parameters,

* Corresponding author.
E-mail address: giuseppe.lacidogna@polito.it (G. Lacidogna).

0013-7944/$ - see front matter © 2013 Elsevier Ltd. All rights reserved.
http://dx.doi.org/10.1016/j.engfracmech.2013.07.011

Nomenclature

A	Acoustic Emission (AE) amplitude
$N(\geqslant A)$	number of Acoustic Emission (AE) signals with amplitude $\geqslant A$
D	fractal dimension
E_r	energy released during an earthquake or Acoustic Emission event
m	Acoustic Emission amplitude A in logarithm scale ($m = \mathrm{Log}_{10}A$)
b	called "b-value", is the negative slope of the $\mathrm{Log}N(\geqslant A)$ vs. m relation
g	coordinate in the origin in the $\mathrm{Log}N$ vs. m diagram
$N(\geqslant E_r)$	number of events with value $\geqslant \mathrm{Log}E_r$
α	adjustment coefficients in the $\mathrm{Log}N(\geqslant \mathrm{Log}E_r)$ vs. $\mathrm{Log}E_r$ relation
ω	adjustment coefficients in the $\mathrm{Log}E_r$ vs. $\mathrm{Log}A$ relation
Δ	increment
E_e	elastic energy stored in the body during the fracture process
E_d	energy dissipated in the fracture process
E_k	kinetic energy evaluated during the fracture process
L	length of the side of the cubic module in the lattice model used
A_l and A_d	cross-sectional areas of the longitudinal and diagonal elements respectively in the lattice model used
ϕ, η	coefficients that let to compute the transversal area of the elements and the length L
v	the Poisson's ratio
$\mathbf{x}$, $\dot{\mathbf{x}}$ and $\ddot{\mathbf{x}}$	vectors that contain the nodal displacements, velocities and accelerations, respectively
$\mathbf{M}$ and $\mathbf{C}$	mass and damping matrices
$F_r(t)$ and $\mathbf{P}(t)$	the internal and external nodal load vectors
t	time
C_p	propagation velocity of longitudinal waves
E	the longitudinal elastic module
S	fracture area of a solid cube of side L
F	elemental axial force in truss-like discrete element model
ε	strain
ϑ	energy dissipated by the fracturing process of a solid cube, due to a crack parallel to one of its faces
G_f	specific fracture energy
A_i^*	equivalent fracture area of each element is defined in order to satisfy the condition that the energies dissipated by fracture of the continuum and by its discrete representation are equivalent. ($i = l$ indicates a longitudinal bars, i:d indicates diagonal bars)
ε_p	critical failure strain defined as the largest strain attained by the element before the initiation of damage
ε_r	limit strain, where the element loses its load carrying capacity
R_f	failure factor, which may account for the presence of an intrinsic defect of size a
a	the intrinsic defect of size into the element in the lattice model
Y	dimensionless parameter that depends on both the specimen and crack geometry
K_r	failure coefficient that relates the critical strain ε_p with the limit strain ε_r ($\varepsilon_r = K_r\varepsilon_p$)
L_{cr}	value of the elemental length L when $K_r = 1$
β and γ	scale and shape parameters in the Weibull distribution function
Ω	Weibull type probability distribution function
$\Gamma(x)$	Gamma function
μ	mean value
s	standard deviation
u	random number with a uniform probability distribution in the [0,1] interval
CV	coefficient of variation
P_{max}	maximum value reached by the load
δ_r	displacement when the rupture takes place
h	value of acceleration computed in the numerical simulation
h_o	reference value of acceleration computed in the numerical simulation that let to normalize the magnitude of the AE events obtained numerically
A_{thres}	relative AE magnitude threshold considered in the compute of the b-values using the results obtained in the simulation
N_{inst}	rate of the AE events
t_f	time when the collapse takes place
$E_k(t_i)$, $E_d(t_i)$	kinetic and damaged energy during the simulation measured in specific time t_i
t_F	instant at which the typical drop in the potential energy occurs during the simulation process
t_{Fa} and t_{Fb}	times in which the potential energy drops during the simulation
χ, λ, θ, τ	adjusting coefficients

c_{Ed} and c_{Ek}	estimations of the c coefficient
d_{Ed} and d_{Ek}	estimations of the d coefficient
f_c	fundamental frequency of vibration related to the longitudinal bars in the truss-like discrete element model used
T_c	fundamental period of vibration related to the longitudinal bars in the truss-like discrete element model used
t_{max}	last time captured during the simulation. This value was used to normalized the simulation process time

such as arrival time, velocity, amplitude, duration and frequency are recorded from the signals. From these parameters the damage conditions and location of the AE sources are determined [14].

Moreover, using the AE technique, an effective damage assessment criterion is obtained from the statistical analysis of the AE signals amplitude distribution that emerges from the growing microcracks. The amplitudes of such signals are distributed according to the Gutenberg–Richter (GR) law, $N(\geqslant A) \propto A^{-b}$, where N is the number of AE signals with amplitude $\geqslant A$. The exponent b of the GR law, the so-called b-value, changes with the different stages of damage growth: the initially dominant microcracking generates a large number of low-amplitude AE signals, while the subsequent macrocracking generates fewer signals, but of higher amplitude. This implies a progressive decrease in the b-value as the specimen approaches impending failure: this is the core of the so-called "b-value analysis" used for damage assessment [4–10,12,15].

On the other hand, the damage process is also characterized by a progressive localization identified through the fractal dimension D of the damaged domain. It is possible to prove that $2b = D$ [3,10,16,17]. Therefore, it is possible to identify the energy release modalities in a structural element during the AE monitoring process by determining the b-value. The extreme cases envisaged are $D = 3.0$, which corresponds to the critical conditions $b = 1.5$, when the energy release takes place through small defects homogeneously distributed throughout the volume; and $D = 2.0$, which corresponds to $b = 1.0$, when energy release takes place on a fracture surface. In the former case, diffused damage is observed, whereas in the latter, two dimensional cracks are formed leading to the separation of the structural element.

A classical energy–magnitude relation, adjusted using earthquake data, was proposed in seismology by Ritcher [18]. This empirical law allows us to affirm that $\mathrm{Log}\, E_r \propto 1.5\, m$, where E_r represents the energy released during an earthquake, and m is the magnitude on the Richter scale. Scholz [19] demonstrated that in many ways the statistical behavior of micro-fracturing activity observed in AE laboratory experiments present the same pattern to that observed for earthquakes; so that the same power-law is valid if we consider the signal trace amplitude measured by AE devices, rather than the seismogram instrumental magnitude.

Finally, it is possible to recognize a typical pattern in terms of signal frequency, which has been determined, among others, by Schiavi et al. [20]: the lowest frequencies of AE signals tend to diminish when the damage process goes from the critical state to collapse.

In this paper, following the presentation of the fundamental theory concerning the b-value, and a brief description of the truss-like discrete element model used to make the numerical simulations, a laboratory uniaxial compression test on a concrete specimen is described. The experimental results are shown in terms of load vs. time diagram, energy balance, classical b-value, alternative b-value computed by the kinetic and dissipated energy rate, and variation of the AE signal frequency analyzed during the fracture process. The results are compared with those obtained by means of the numerical truss-like discrete element model.

2. *b*-Value analysis

Magnitude (m) is a Geophysics log-scale quantity, and it is often used to measure the amplitude of an electrical signal generated by an AE event. The magnitude is related to the event amplitude A, expressed in microvolts (μV), by the equation [4,6,9,10,15]:

$$m = \mathrm{Log}_{10} A. \tag{1}$$

The Gutenberg–Richter (GR) law, initially used in seismicity, it is widely accepted and describes the statistical distribution of AE signal amplitudes [4,6,9,10,15]:

$$\mathrm{Log}\, N(\geqslant m) = g - bm, \tag{2}$$

where N is the number of peaks with magnitude greater than m, while the coefficient b, called "b-value", is the negative slope of the Log N vs. m diagram. Microcracks release low-amplitude AEs, while macrocracks release high-amplitude AEs. This intuitive relationship is confirmed by the experimental result, which shows how the area of crack advancement is proportional to the amplitude of the related AE signal [13].

From Eq. (2) it results that microcracks generate AE events with low magnitudes, and therefore lead to relatively high b-values (raising the threshold m, the number of surviving signals rapidly decays). Instead, when macrocracks start to appear, lower b-values are observed. Therefore the analysis of the b-value, which changes systematically with the different stages of the fracture process [4–10,12,15], has been recognized as a useful tool for damage level assessment.

In general terms, the fracture process moves from micro to macrocracking as the material approaches impending failure and the b-value decreases. When the tested material approaches the peak load, the b-value is found to be around 1.5. Then, it decreases and attains values $\approx$1.0 or less, when the material approaches failure [6,7,9,10,12,15]. Furthermore, as pointed out in Carpinteri et al. [15], the b-value statistical analysis is closely connected to the fractal geometry approach used in the damage mechanics of heterogeneous materials. Fractal geometry can be considered a natural tool to characterize self-organized processes and the scaling laws that arise from the critical points.

3. Relationship between released energy and magnitude

It is possible to write the relation between the released energy, E_r, during a damage process, and the amplitude, A of the AE events, in the following form:

$$E_r = \omega A^c, \tag{3}$$

or, by applying logarithms to both sides:

$$\mathrm{Log}\, E_r = \mathrm{Log}\, \omega + c\, \mathrm{Log}\, A, \tag{4}$$

where ω and c are adjustment coefficients.

From physics it is known that the energy carried by elastic waves is proportional to the square of the signal amplitude; this fact permits to justify $c = 2$ in Eq. (3), and then we could write:

$$E_r = \omega A^2. \tag{5}$$

The first experimental results, taking into consideration Eq. (5), attributed to ω the value of 8.0, but, in this case, the energy associated with earthquakes of low magnitude was underestimated [18]. Afterwards, by adjusting the parameters of Eq. (3) with experimental results obtained from earthquakes of magnitude $m < 7$, Richter proposed the following expressions [18]:

$$E_r = 11.4 A^{1.5}, \tag{6}$$

or

$$\mathrm{Log}\, E_r = 11.4 + 1.5\, \mathrm{Log}\, A. \tag{7}$$

Eq. (6) is closely linked to theoretical studies on the energy released from short distances, such as measured near the epicenter of the seismic phenomenon. Moreover, this relation, if compared with Eq. (5), features an overestimating of the energy released from low-intensity earthquakes. Given the high frequency of earthquakes with magnitude less than $m = 7.0$, earthquakes in the Richter scale magnitude comprised between 6.0 and 6.9 have a frequency approximately of 120 per year on Earth's crust, Eq. (6) is still the most used. However, considering Eq. (5) with $\omega = 8$, and Eq. (6), it can be observed that for $m = 6.8$ the values of the energy supplied by the two equations coincide. In both cases we get: $\mathrm{Log}\, E_r = 21.6$. Therefore, following Richter, to obtain a plausible estimate of the energy released from earthquakes of magnitude greater than $m = 6.8$, it is also possible to use Eq. (5).

Considering Eq. (3), Scholz [19] presented a scale-independent analytical model that can be applied in laboratory tests or seismic events. This model uses strong but plausible hypotheses: (i) it works with anisotropic linear elastic material; (ii) all the cracks are considered of a penny-shape type, and, although they can have different sizes, they must be similar to each other; and (iii) the mean stress applied to the domain is constant. This analytical model allows us to obtain interesting conclusions about the b-value defined above. Among others, the model predicts the tendency of the b-value to decrease when the fracture process develops.

A general discussion about different global parameters commonly applied in seismology is presented in Kanamori and Anderson [21]. They analyzed the relationship between the elastic energy released in an earthquake, E_r, and the signal amplitude, A, and emphasized that not all the increments elastic energy, ΔE_e, are related to the AE events amplitude. A part of these increments is dissipated in the fracture process (ΔE_d), and another part becomes kinetic energy that we call released energy E_r.

As a matter of fact, also in Carpinteri et al. [22], the authors indicated that the AE events, generated by mechanical waves, are directly related to the energy released, E_r, during the damage process. The released energy E_r is correlated to the increments ΔE_d of the energy dissipated during the damage process, but they are not the same. Variations in elastic energy, ΔE_e, that do not produce transient waves, are not detected as AE events.

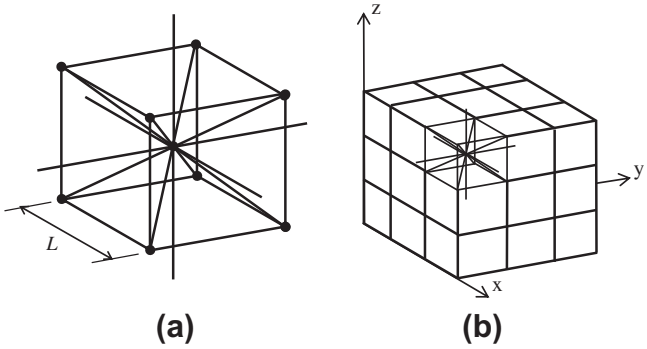

Fig. 1. DEM discretization strategy: (a) basic cubic module and (b) generation of a prismatic body.

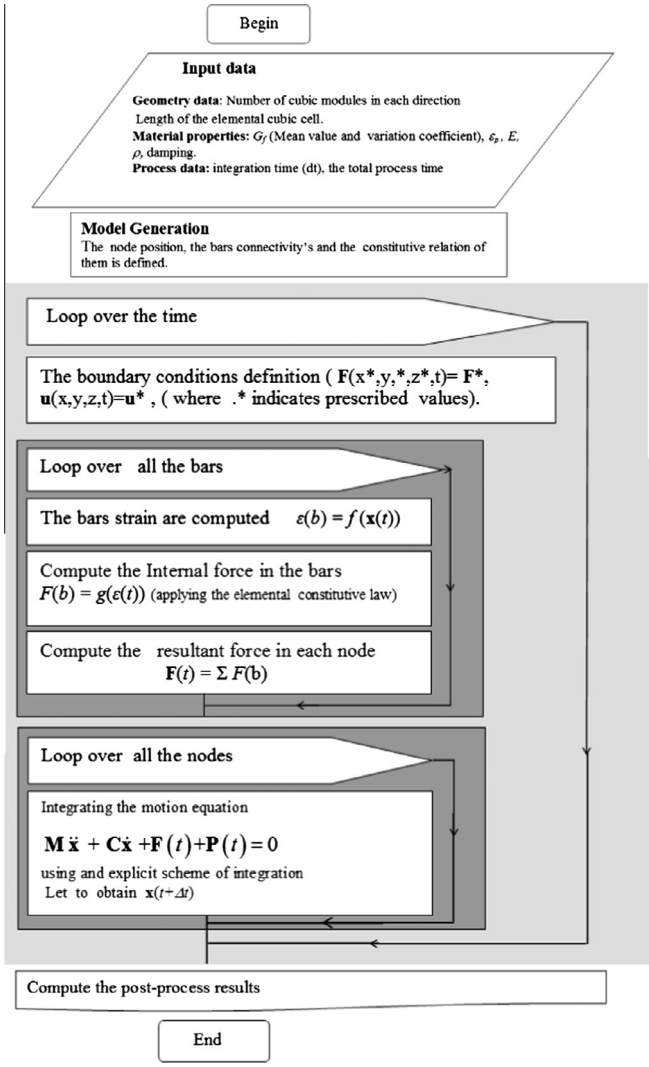

Fig. 2. Flow chart with the DEM algorithm.

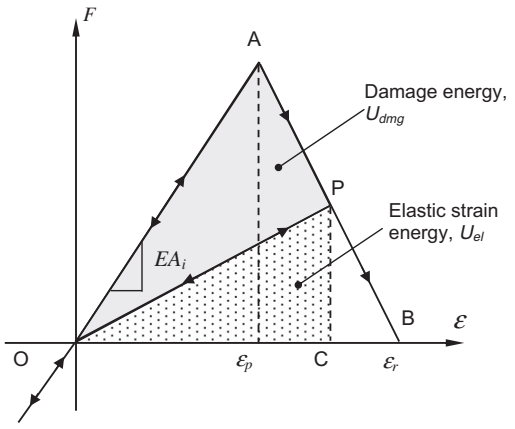

Fig. 3. Bilinear constitutive law adopted for DEM uniaxial elements.

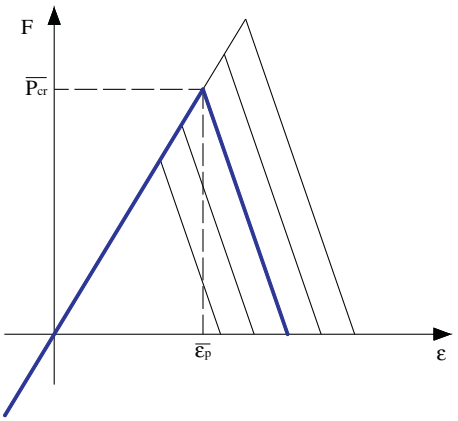

Fig. 4. The constitutive law and its variation when G_f is considered as a random field.

4. Relationship between the released energy and the number of events

In Chakrabarti and Benguigui [23], the relationship between the number of events $N(\geqslant E_r)$ and the released energy E_r was also shown in the following form:

$$\mathrm{Log}\, N(\geqslant \mathrm{Log}\, E_r) = \mathrm{Log}\,\alpha - d\,\mathrm{Log}\,(E_r). \tag{8}$$

As mentioned in [23], the expected d value in the seismology context must fall between 0.8 and 1.1. Moreover, it is easy to verify that by combining Eqs. (2) and (8), we obtain Eq. (3), where the coefficient $c = b/d$.

The fundamental relations discussed in Sections 2–4 are in perfect agreement with the results obtained by means of the DEM truss-like discrete element model simulation presented in this work, in which the correlation between the Acoustic Emission signals amplitude A, the number of events N, and the measurement of the released energy E_r during the simulation are analyzed.

5. Truss-like Discrete Element Method (DEM)

In the truss-like discrete element model used here, (DEM), a continuum is represented by a set of lumped masses interconnected by a set of unidimensional elements or *bars*. Fig. 1a and b presents the discretization of a cubic system, for which the stiffness of the DEM elements, corresponding to an equivalent orthotropic linear elastic material, were obtained according to Nayfeh and Hefzy [24].

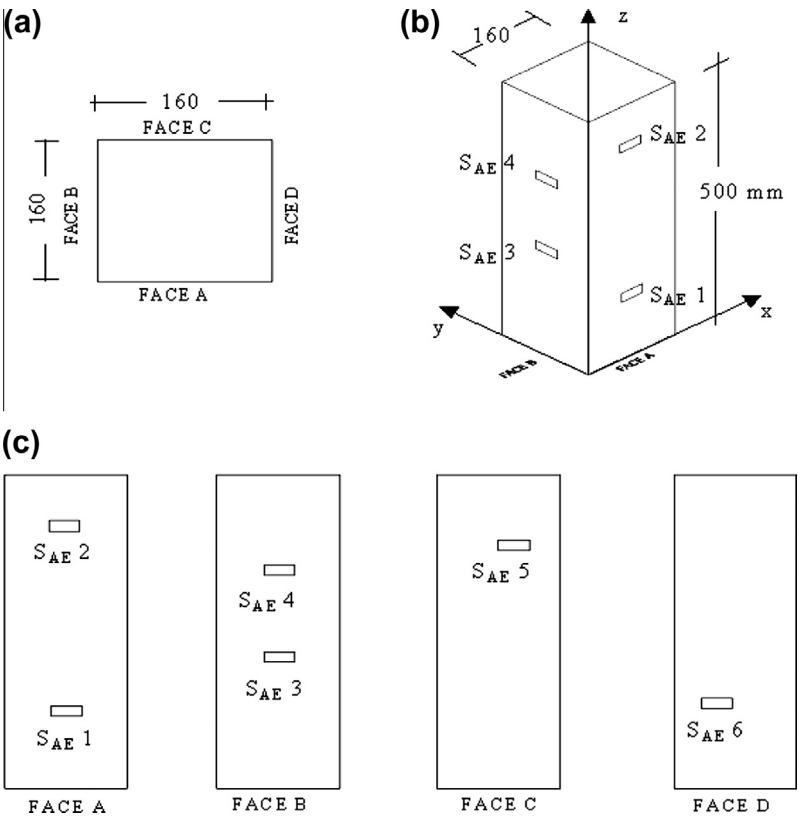

Fig. 5. Concrete specimen in compression. (a) Cross-section of the specimen. (b) Assonometric projection with the positioned AE sensors. (c) Overview of the four specimen faces.

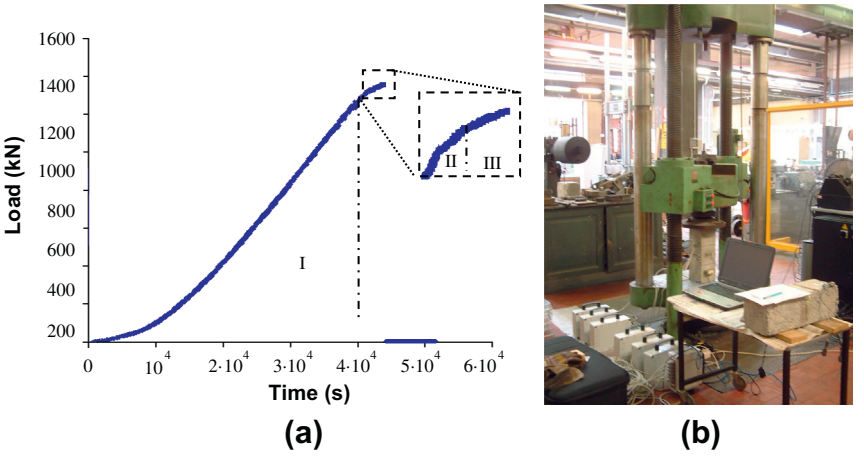

Fig. 6. Concrete specimen in compression. (a) Load–time diagram of the test performed in displacement control mode. The specimen failed in a quasi-brittle manner: in region I, where linear elasticity is valid, there is little damage (i.e., low-amplitude AE events), while in regions II and III, damage results in a deviation from linear elasticity and an increase in the AE level. (b) Photo of the MTS machine and of the specimen during the test. The devices utilized to detect the AE signals can be observed on the left.

The basic cubic module has 20 elements and 9 nodes. Each node has three degrees of freedom, namely the three components of the displacement vector in a global reference system. In the case of an isotropic elastic material, the cross-sectional area A_l of the longitudinal elements (those defining the edges of the module, and those parallel to the edges connected to the node located in the center of the module) in the equivalent discrete model is:

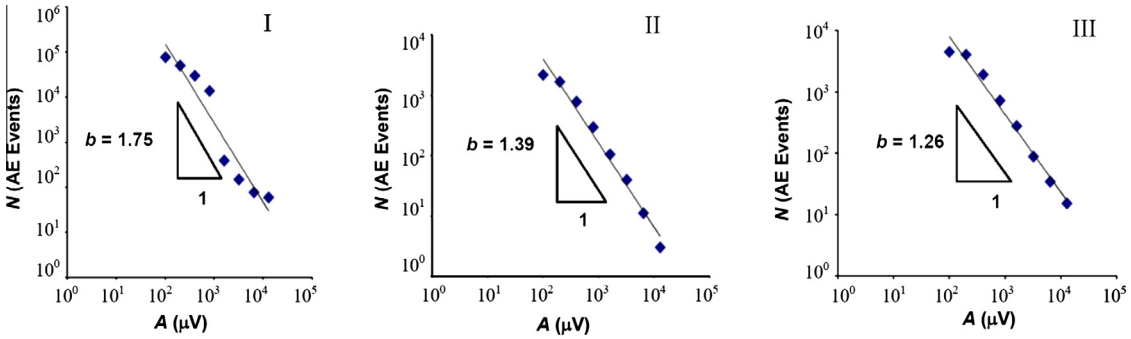

Fig. 7. Concrete specimen in compression: *b*-values during the three stages of the loading test. It should be pointed out that the event amplitudes *A* are reported in the *x*-axis, instead of the magnitudes *m*.

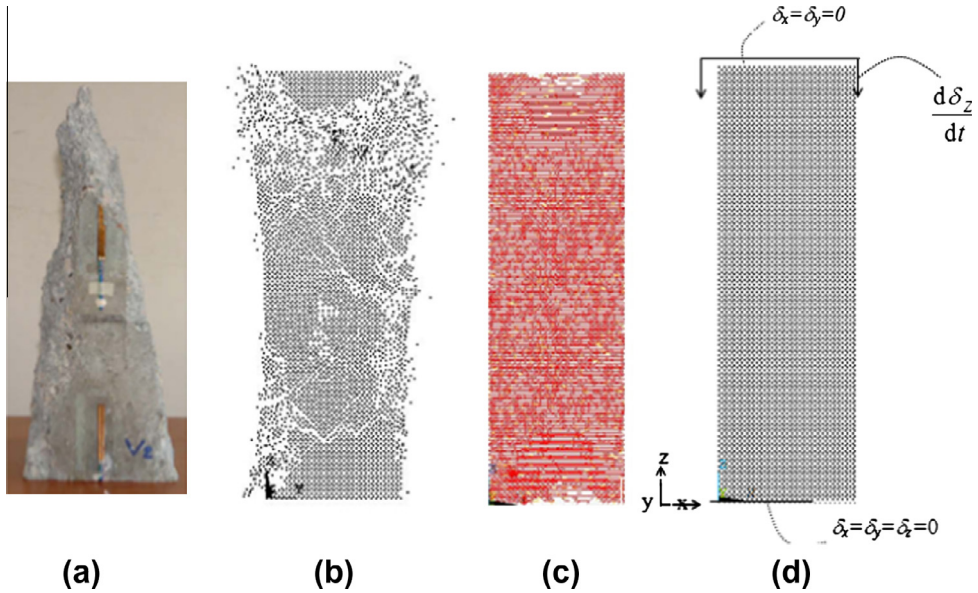

Fig. 8. (a) Experimental rupture configuration. (b) Numerical rupture configuration, plotting of the nodes. (c) Plotting of the fractured elemental bars near total collapse. (d) Initial configuration in which the applied boundary conditions are shown.

Table 1
Main mechanical properties adopted in the DEM simulation.

E (elastic Young's modulus) = 9 GPa
ρ (density) = 2500 kg/m^3
$\mu(G_f)$ = 560 N/m (mean value), $CV(G_f)$ = 50%
$\mu(\varepsilon_p)$ (mean critical strain) = 2.4×10^{-4}

$$A_l = \phi L^2, \tag{9}$$

where L is the length of the side of the cubic module under consideration. Similarly, the area A_d of the diagonal elements is:

$$A_d = \frac{2}{\sqrt{3}}\eta\phi L^2. \tag{10}$$

It should be noted that there is a difference in length between the longitudinal and diagonal elements, since:

$$L = (2/\sqrt{3})L_d. \tag{11}$$

For isotropic solids:

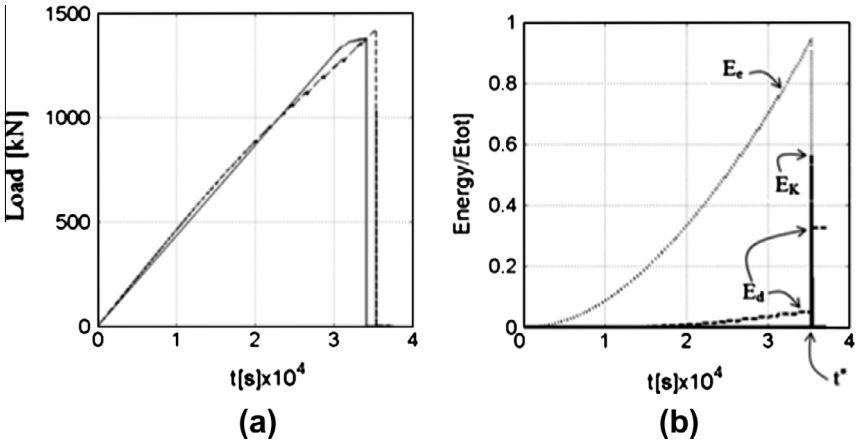

Fig. 9. (a) Load vs. time, comparison between the experimental (continue line) and numerical simulation (dashed line). (b) Normalized energy balance vs. time (E_e: elastic energy; E_k: kinetic energy; E_d: dissipated energy; $E_{tot} = E_e + E_k + E_d = 2495$ Nm at t^*).

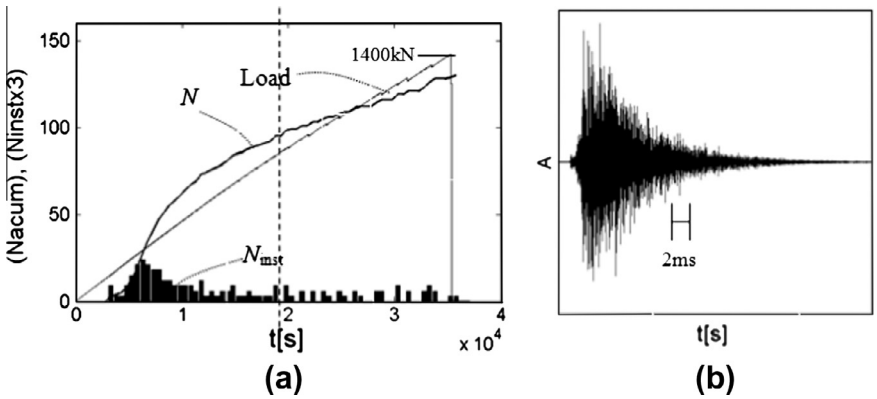

Fig. 10. Numerical results. (a) Load vs. time diagram, cumulated AE events (N) and AE event rate (N_{inst}) vs. time. (b) Typical AE signal obtained numerically.

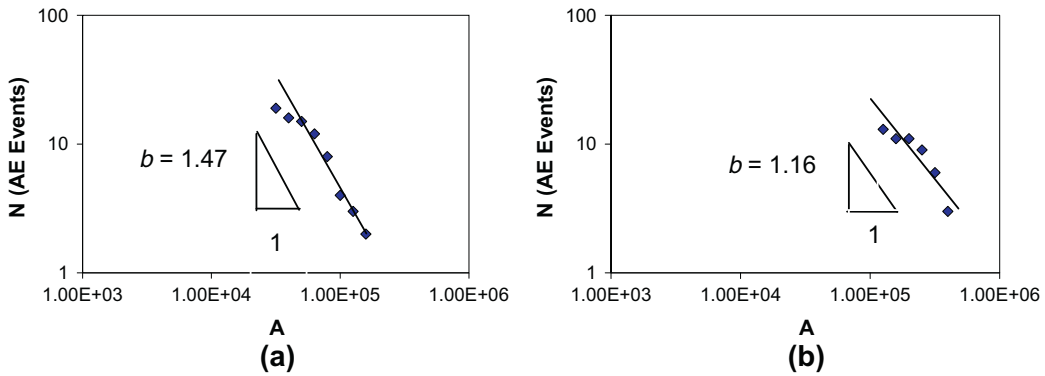

Fig. 11. Numerical results for the concrete specimen under uniaxial compression: b-values computed during the simulation, (a) [0, 18,000] s interval and (b) [18,000, t_f] s interval. The event amplitudes in the diagrams are represented by normalized unity A, while N represents the cumulated AE events.

$$\phi = (9 + 8\eta)/(18 + 24\eta), \tag{12}$$

$$\eta = 9\nu(4 - 8\nu), \tag{13}$$

where ν is Poisson's ratio. The correspondence between the equivalent discrete solid and the isotropic continuum is complete for $\nu = 0.25$. On the other hand, small discrepancies appear in the shear terms for values of $\nu \neq 0.25$, which nevertheless

may be neglected. It is interesting to note that, while truss-like model cannot precisely represent a *locally* isotropic continuum, it can also be argued that no perfect *locally isotropic continuum exists* in the physical world. In fact, continuum itself does not exist. Isotropy in solids is a bulk property that reflects the properties of the random distribution of the orientation of the elements. The derivation of the areas of longitudinal and diagonal elements is given for a cubic array by Eqs. (9) and (10) as reported in [24–26].

The equations of motion are obtained from equilibrium conditions of all the forces acting on the nodal masses, which result in a system of equations with the form:

$$\mathbf{M}\ddot{\mathbf{x}} + \mathbf{C}\dot{\mathbf{x}} + \mathbf{F}(t) + \mathbf{P}(t) = 0, \tag{14}$$

in which x, $\dot{x}$ and $\ddot{x}$ denote the vectors that contain the nodal displacements, velocities and accelerations, respectively, while **M** and **C** are the mass and damping matrices. The vectors $\mathbf{F}(t)$ and $\mathbf{P}(t)$ contain the internal and external nodal loads.

Since matrices **M** and **C** are diagonal, the terms in Eq. (14) are not coupled, and can easily be integrated in the time domain using an explicit finite difference scheme. It is worth noting that, since nodal coordinates are updated at each time step, large displacements are accounted for naturally. Stability of the integration scheme is guaranteed by adopting a time interval Δt in the integration process so that:

$$\Delta t \leqslant \frac{0.6L}{C_P}, \tag{15}$$

in which C_p is the propagation velocity of longitudinal waves,

$$C_P = \sqrt{E/p}. \tag{16}$$

The convergence of DEM solutions in linear elasticity and elastic instability problems has been verified by Dalguer et al. [26], among others. In Fig. 2 a general flow chart helps to understand the algorithm.

6. Non-linear constitutive model for material damage

Riera [27] and Rios and Riera [28] adopted the softening law for quasi brittle materials proposed by Hillerborg [29] and extended the Discrete Element Model to deal with brittle fracture by means of the bilinear constitutive relationship (*ECR*) shown in Fig. 3, which allows to account for the irreversible effects of crack nucleation and propagation, and therefore, predicts the reduction in the element load carrying capacity due to damage. The area under the force vs. strain curve (the area of triangle *OAB* in Fig. 3) represents the necessary energy density to fracture the area of influence of the element. Thus, for a given point *P* on the force vs. strain curve, the area of the triangle *OPC* represents the reversible elastic energy density stored in the element, whereas the area of triangle *OAP* is the energy density dissipated by damage. Once the damage energy density is equal to the fracture energy, the element fails and loses its load carrying capacity. Instead, in the case of compressive loads, the behavior of the material is assumed linearly elastic. Thus, failure in compression is induced only by indirect traction.

The constitutive parameters and symbols are shown in Fig. 3 [30]. The axial force F of the element depends on the axial strain ε. The area associated to each element is given by Eqs. (9) and (10) for longitudinal and diagonal elements, respectively. An equivalent fracture area A_i^* of each element is defined in order to satisfy the condition that the energies dissipated by fracture of the continuum and by its discrete representation are equivalent. To this aim, fracturing of a cubic sample of dimensions $L \times L \times L$ is considered. The energy dissipated by fracturing of a continuum cube, due to a crack parallel to one of its faces, is:

$$\vartheta = G_f S = G_f L^2, \tag{17}$$

in which S is the actual fractured area, i.e. L^2. On the other hand, the energy dissipated when a DEM module of $L \times L \times L$ dimensions fractures into two parts, which consist of the contributions of five longitudinal elements. More details about this topic could be founded in [39].

The *critical failure strain* (ε_p) is defined as the largest strain attained by the element before the initiation of damage (point A in Fig. 3). The relationship between ε_p and the specific fracture energy G_f is given in terms of Linear Elastic Fracture Mechanics as:

$$\varepsilon_p = R_f \sqrt{\frac{G_f}{E(1-\nu^2)}}, \tag{18}$$

in which R_f is the so-called failure factor, which may account for the presence of an intrinsic defect of size a. R_f may be expressed in the following terms:

$$R_f = \frac{1}{Y\sqrt{a}}, \tag{19}$$

in which Y is a dimensionless parameter that depends on both the specimen and crack geometry. The element loses its load carrying capacity when the *limit strain* ε_r is reached (point C in Fig. 3). This value must satisfy the condition that, upon failure

of the element, the dissipated energy density equals the product of the element fracture area A_i^* times the specific fracture energy G_f, divided by the element length. Hence:

$$\int_0^{\varepsilon_r} F(\varepsilon)d\varepsilon = \frac{G_f \cdot A_i^*}{L_i} = \frac{K_r \cdot \varepsilon_p^2 \cdot E \cdot A_i}{2}, \tag{20}$$

in which the sub index i is replaced by l or d, depending on whether the element under consideration is longitudinal or diagonal. The coefficient K_r is a function of the material properties and the element length L_i:

$$K_r = \left(\frac{G_f}{E\varepsilon_p^2}\right)\left(\frac{A_i^*}{A_i}\right)\left(\frac{2}{L_i}\right). \tag{21}$$

In order to guarantee the stability of the algorithm, the condition $K_r \geqslant 1$ must be satisfied [31].

An expression of the limit strain is:

$$\varepsilon_r = K_r \varepsilon_p. \tag{22}$$

It is also worth noting that, although the DEM uses a scalar damage law to describe the uniaxial behavior of the elements, the global model accounts for anisotropic damage since it has elements orientated in different spatial directions.

Finally, note that the so-called truss elements simply serve to visualize the direction of forces between two nodal masses, and are thus mainly useful for engineering calculations. They do not exist physically (the truss elements are massless). The complete "failure" of an element simply implies that there are no forces acting between the corresponding interconnected nodes, and it does not mean that there is "fracture" unless all truss elements that cross a measurable surface are broken.

7. Random distribution of the material parameters in the DEM environment

Rocha et al. [30] introduced the possibility of considering the toughness in DEM as a random parameter. They defined the toughness G_f with a Weibull type probability distribution, using the two parameters given from the following expression:

$$\Omega(G_f) = 1 - \exp[-(G_f/\beta)^{\gamma}], \tag{23}$$

where β and γ are the scale and shape parameters, respectively. It is possible to verify that the following expressions allow us to define the mean value (μ) and the standard deviation (s):

$$\mu = \beta[\Gamma(1 + 1/\gamma)], \tag{24}$$

$$s = \beta[\Gamma(1 + 2/\gamma) - \Gamma^2(1 + 1/\gamma)]^{1/2}, \tag{25}$$

where $\Gamma(x) = \int_0^{\infty} t^{x-1}e^{-t}dt$ is a *Gamma* function.

If we wish to simulate pseudo random values of G_f, it is possible to use, the following expression:

$$G_f = \beta[-\ln(1 - u)]^{1/\gamma}, \tag{26}$$

where u is a random number with a uniform probability distribution in the [0,1] interval. The correlation length of the random field simulated in the simplest formulation of DEM was obtained considering that the correlation length of the random field is a function of the basic DEM element.

This constitutes a very important limitation because, if the discretization level is changed, the characteristics of the random field are changed. However, it is now possible for the correlation length of the random field to become independent from the discretization level (see [32] for the implementation procedure). A scheme showing the constitutive law variations among the bars of the model is presented in Fig. 4.

The incorporation of the random nature in the properties also lets to avoid the influence of the regular lattice mesh in the response.

This version of truss-like discrete element model, called here DEM, has been successfully used to solve structural dynamics problems, such as shells subjected to impulsive loading [33,34], fracture of elastic foundations on soft sand beds [35], recreation of the generation and subsequent spread of an earthquake [25,26], the study of the scale effect in concrete [28], and in rock dowels, [36,37], the computation of fracture parameters in static and dynamic problems [38–40], and in the study of Strength of Brittle Materials under High Strain Rates [41]. Based on these references, we consider the DEM a good numerical alternative to simulate the acoustical emission in the following application. Similar approach using other version of truss-like discrete element model could be consulted in [42–44].

8. Concrete prismatic specimen subject to uniaxial compression

A concrete specimen in compression was investigated through AE monitoring in a laboratory test. The concrete, of good mechanical properties, characterized by a compressive strength comprised between 50 and 60 MPa, presents an apparent specific weight of about 2.38 g/cm^3 and a maximum aggregate size of about 15 mm. The water-cement ratio is limited in

0.38, while the cement content is of about 320 kg/m^3. The concrete was made according to the European UNI EN 206-1: 2006 and UNI EN 1992-1-1: 2005 rules. This specimen is part of a group specifically realized for this kind of tests.

Six AE transducers (indicated as S_{AE} 1 to S_{AE} 6) were placed on the surface of the specimen, a prism measuring $160 \times 160 \times 500$ mm^3 (see Fig. 5) [14]. The test has been performed in displacement control mode using an electronic controlled Servo-hydraulic Material Testing Systems machine (MTS 311,31 model), with a capacity of 1800 kN, and imposing a constant rate of displacement on the upper loading platen: the displacement rate in the first 10^4 s was $d\delta/dt = 10^{-5}$ mm/s, and it was then increased to 10^{-4} mm/s up to failure.

This kind of machine is controlled by an electronic closed-loop servo-hydraulic system (Fig. 6b). It is therefore possible to perform tests under load or displacement control. The displacements are recorded by four strain gauges (HBM 1-LY41-50/120 model) placed on the specimen surface. In spite of the low value chosen for the displacement rate, the specimen has failed in a brittle manner, as can be seen in the load vs. time (strain) diagram in Fig. 6a, where the linear branch extends over almost the entire duration of the test.

The characterization of the fracture process was carried out using the *b*-value analysis. The loading test was divided into three stages: the first stage, where linear elasticity was still valid, and two subsequent stages characterized by deviations from linear elasticity and the existence of damage. The *b*-value calculated at the earliest stage of the loading test, where linear elasticity was still valid, was 1.75, an index of a low damage level. The *b*-values calculated in the two following stages of the damage region were 1.39 and 1.26, respectively, confirming the decreasing trend of the *b*-value as the damage developed (Fig. 7). The final configuration of the specimen after testing is shown in Fig. 8a.

9. The implemented numerical model

The numerical model of the specimen was built with $27 \times 27 \times 86$ cubic modules. Each cubic module has a side length of $L = 6$ mm, therefore the model contains 13×10^4 nodes, and 88×10^4 elemental bars. Using the load vs. time diagram, and the information described in Section 8, an initial elastic modulus of $E = 9$ GPa was obtained. This value of E is lower than the classical value of concrete (normally 35–40 GPa). This is due to the fact that the specimen had been subjected to a pre-damage process before the main test was carried out. The specimen was subjected to a uniform compression load up to 1300 kN for two consecutive days, and then unloaded. During the main test, the damaged specimen was reloaded up to collapse by applying the displacement rates indicated in Section 8, and AE sensors monitored it. The material properties summarized in Table 1 were used in the DEM simulation. The experimental results, in terms of load vs. time diagram, are reported in Fig. 6a and in Fig. 9a.

The parameter G_f is directly proportional to the area below the force vs. strain diagram presented in Fig. 3. A layout of the model and the applied boundary conditions are presented in Fig. 8d. The parameter G_f is defined as a random field with the mean and variation coefficient, presented in Table 1, using a probability Weibull density distribution. In this numerical implementation, the level of discretization employed ($L = 6$ mm) is directly linked with correlation length of the random field of G_f, associated with the grain size of the material. About the computation time required for numerical simulations on similar problems presented in this work, it is in the order of 10 h for a normal desktop. On the other hand, it is easy to apply vectorization and parallelization techniques in DEM algorithms if we need to compute heavier models.

The relationship between the variation coefficient of the random field G_f and the critical strain ε_p are represented by the following equation:

$$CV(\varepsilon_p) = 0.5CV(G_f). \tag{27}$$

A virtual sensor was located in the position indicated in Fig. 5 (S_{AE} 1). The perpendicular acceleration of the sensor surface was captured by the same virtual sensor, and interpreted as a measure of the AE signals. A typical captured signal is shown in Fig. 10b. The numerical simulation was carried out using the fastest displacement rate prescribed in the experimental test, taking care not to introduce important inertial effects. This can be verified in Fig. 9b, which presents the energy balance calculated during the simulation. The kinetic energy represented in this plot has very low values until the catastrophic specimen collapse.

10. Numerical results

10.1. Final configuration, load and energy vs. time

The experimental and numerical specimen configuration pertaining to the end of the test are shown in Fig. 8a and b, respectively. In these plots, it is possible to appreciate that the upper sections of the specimen are the most damaged, and that cone-shaped ruptures have occurred in the proximity of the ends of the specimen. This is due to the confinement of the transversal displacements at both ends (see Fig. 8d).

The fractured bars close to the final specimen collapse are plotted in Fig. 8c. In this figure it is shown how the main fracture mechanism occurs when the ultimate strength is reached with the transversal (perpendicular to the load direction) bars in traction.

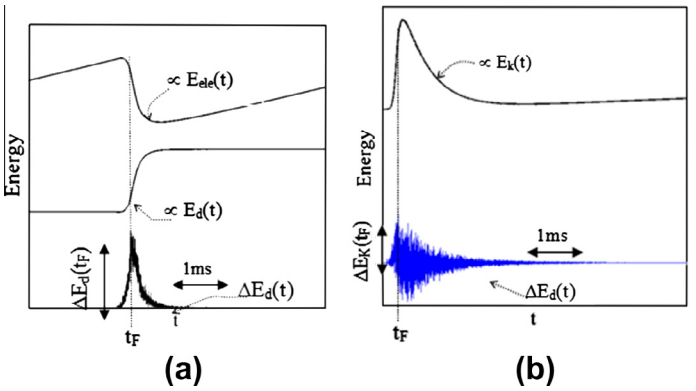

Fig. 12. (a) Variations in time of the dissipated energy increments ΔE_d, the dissipated energy E_d and the elastic energy E_{ele} during the entire simulation process. (b) Variations in time of the kinetic energy increment ΔE_k and kinematic energy E_k during the entire simulation process.

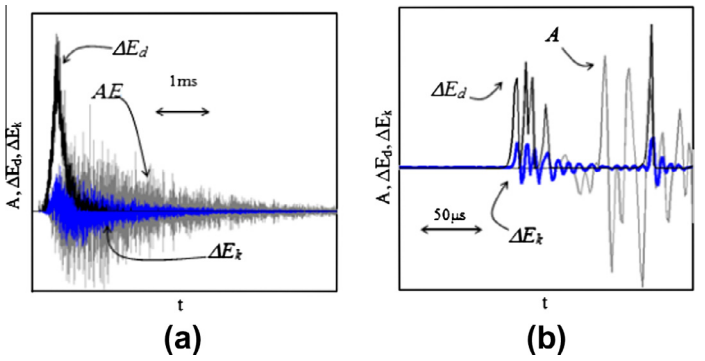

Fig. 13. (a) The three types of signals overlapped. The signal amplitudes have been modified in order put them all in the same scheme. (b) Details of the beginning of the peak event. Increment in dissipated energy $\Delta E_d(t)$, increment in kinetic energy $\Delta E_k(t)$, and the irradiated AE signal.

A comparison between experimental test and numerical simulation, in terms of load vs. time diagrams, is shown in Fig. 9a. The peak loads and the areas of the plotted curves present a good correlation, but there are some differences between the way the experimental and numerical specimens reach the collapse. In the experimental curve, the loss of linearity near the peak load shows that the maximum amount of damage occurred in the last part of the diagram. A sharp drop in stress has taken place in the simulation curve in the second part of the process.

The elastic energy stored in the specimen, the dissipated energy and the kinetic energy of the system are shown in Fig. 9b. The three quantities are computed over all the parts of the system, at each integration step, by means of the motion equation presented in Eq. (14). The kinetic energy shows very low values up to the abrupt collapse, as can be observed in Fig. 9b. This confirms that negligible inertial effects appear during the simulation.

In order to obtain an overall verification of the numerical results, the maximum elastic energy stored in the specimen could be computed using the experimental values in the following way:

$$E_e = (1/2)P_{max}\delta_r, \tag{28}$$

where $P_{max} = 1400$ kN, as provided in Figs. 5 and 8, while the maximum displacement could be computed as follows: $\delta_r = (d\delta/dt)(t_r) = 10^{-5}$ mm/s $\times$ 34,000 s = 3.4 mm.

We thus obtain:

$$E_e = (1/2)(3.4 \times 10^{-3}\ \text{m})(1400\ \text{kN}) = 2380\ \text{Nm}. \tag{29}$$

As shown in Fig. 8b, the maximum value for the elastic energy stored during the experimental test is ≈2500 Nm, which is compatible with the 2380 Nm obtained numerically. It is possible to carry out this simplified verification because, in the present case, the behavior of the body is approximately linear up to collapse.

It is important to emphasize that the truss-like discrete element model used in this version has the ability to simulate problems in which the traction solicitation is dominant, and in particular specimens of quasi-brittle material subjected to pure traction, shear or bending, in which the main rupture mechanism is due to traction. If the sample is under compression,

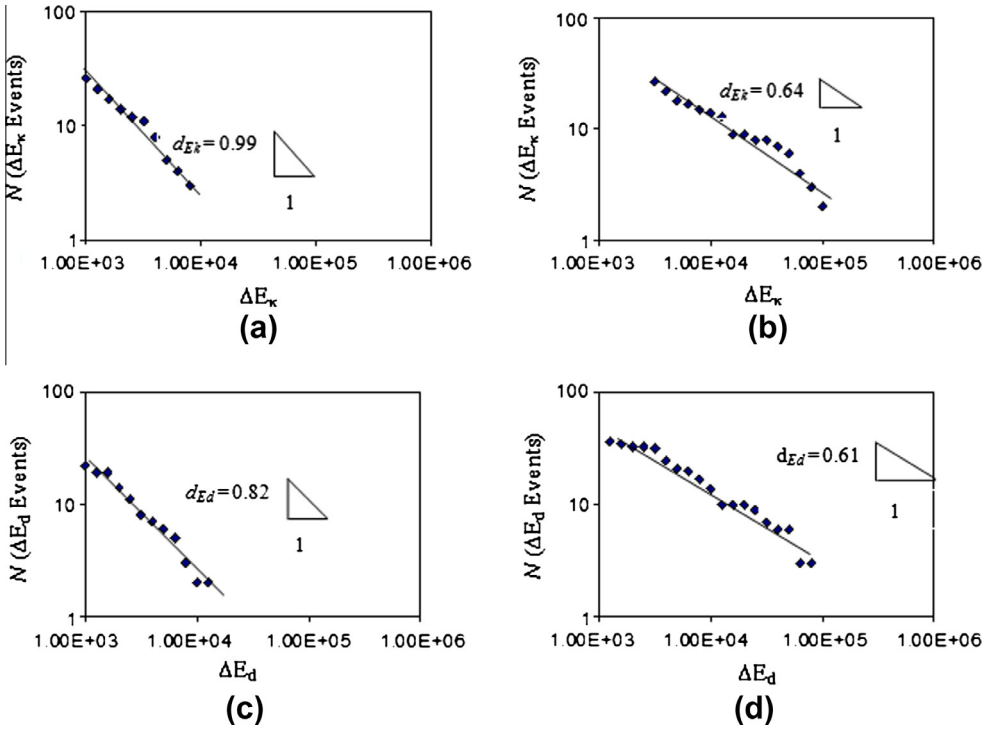

Fig. 14. Numerical results for the concrete specimen in compression: d-values during the two loading test stages. Using increments of kinetic energy, (a) in the [0,18,000] s interval, and (b) in the [18,000, t_f] s interval. Using increments of dissipated energy, (c) in the [0,18,000] s interval, and (d) in the [18,000, t_f] s interval. In the plots, N represents the cumulated events, while ΔE_d and ΔE_k represent the energy magnitudes in normalized units.

as in the analyzed case, it is also possible to correctly simulate its behavior up to the peak load. In this case rupture occurs for indirect traction of the transversal bars (see Fig. 8c).

Nevertheless, it is not possible to capture the typical softening behavior that appears in compression tests after the peak load, with the present model. In the analyzed example, this numerical limitation did not affect the quality of the simulation, because the specimen did not show a softening branch, but instead showed brittle behavior with a snap-back virtual branch.

10.2. b-Value computation

The load vs. time curve, the cumulated AE events, N, and the AE event rate, N_{inst}, are represented in Fig. 10a. The relative signal amplitudes were computed to represent these diagrams (we defined $A = h/h_o$, where $h_o = 100$ mm/s^2). Then, only signals with greater amplitudes than the predetermined threshold $A_{thres} = h/h_o = 500$ were taken into account.

The clearly different behavior in the N and N_{inst} curves allows us to define two time intervals for the b-value analysis: [0,18,000] s and [18,000, t_f] s, where t_f is the moment of the final collapse. The dashed vertical line which can be observed in Fig. 10a indicates the point of separation between these two intervals, while a typical AE event obtained during the simulation is shown in Fig. 10b.

The b-values obtained in the two intervals are represented in Fig. 11a and b. The b-values obtained in the numerical simulation present a decreasing trend during the advancement of the damage process, and are compatible with the experimental ones. Moreover, numerical b-values fall between the limits indicated by Carpinteri et al. [14], that is, $b = 1.47$ for the first interval, and $b = 1.16$ for the second. The differences between the experimental and numerical b-values can be explained by

Table 2
Computed b, d and c values using AE, ΔE_d and ΔE_k.

Time interval	[0,18,000] s	[18,000, t_f] s
AE	$b = 1.47$	$b = 1.16$
ΔE_d	$d_{Ed} = 0.82$ $c = b/d_{Ed} = 1.79$	$d_{Ed} = 0.61$ $c = b/d_{Ed} = 1.90$
ΔE_k	$d_{Ek} = 0.99$ $c = b/d_{Ek} = 1.48$	$d_{Ek} = 0.64$ $c = b/d_{Ek} = 1.81$

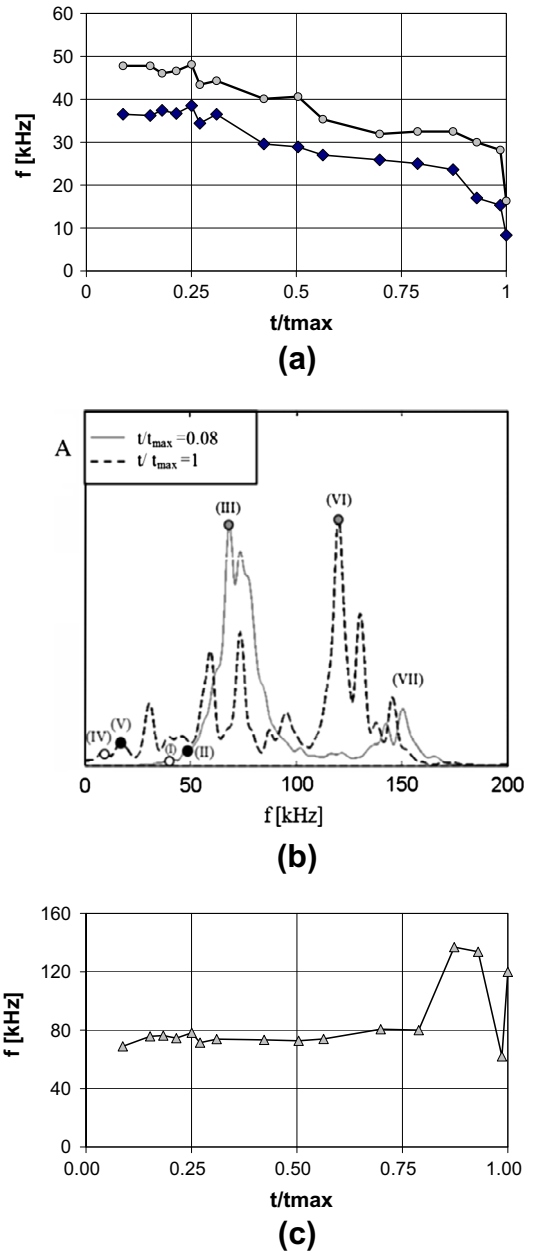

Fig. 15. (a) Evolution of the two lower frequencies during the fracture process. (b) The signal spectrum at the beginning of the test (t/t_{max} = 0.08), and at the final collapse (t/t_{max} = 1), the two lower frequencies in each curve were marked in this plot. (c) Evolution of the peak frequency during the fracture process.

the following reasons: (i) The pre-damage process before the main test was carried out (see Section 9) creates a complex initial condition that could not be adequately considered in the numerical model. (ii) Due to limitations of the numerical model, in applying the prescribed loading rate, a quantity of virtual AE events that do not correspond exactly to the experimental ones were produced.

All the signals utilized for the *b*-values calculation in the numerical simulation had higher amplitudes than the fixed threshold A_{thres} = 500. Because of this choice, only a few events were analyzed in the simulation. Moreover, by applying a lower imposed displacement rate, and considering a lower value of the fixed threshold, it would be possible to identify more isolated AE peaks, especially in the first part of the process.

Considering these AE events in the *b*-value analysis, two negative slopes of the peak-amplitude distribution appear for each time interval, and the first one is about one-fifth of the main *b*-value. This pattern indicates the presence of precursors, i.e. small events warning that a large event is about to occur. A future work will focus on a deep study of this aspect.

10.3. Relationship between AE events and energy parameters

In the present section, the relationship between the released energy, E_r, during the fracture process and the signal amplitude, A, is analyzed. Considering [23], E_r is associated with drops in the potential energy evaluated during the damage process. With the aim of capturing the energy E_r in the DEM context, we propose to compute the increments in dissipated and kinetic energy between two successive integration times, as shown by the following expressions:

$$\Delta E_d(t_i) = E_d(t_i) - E_d(t_{i-1}), \tag{30}$$

$$\Delta E_k(t_i) = E_k(t_i) - E_k(t_{i-1}), \tag{31}$$

where E_d and E_k are the dissipated and kinetic energy in the discretized time during the simulation.

We assume the validity of the following relation:

$$\frac{\Delta E_d(t_{Fa})}{\Delta E_d(t_{Fb})} = \frac{\Delta E_k(t_{Fa})}{\Delta E k_k(t_{Fb})} = \frac{E_r(t_{Fa})}{E_r(t_{Fb})}, \tag{32}$$

where t_{Fa} and t_{Fb} are the times in which the potential energy drops during the simulation.

In this way, Eq. (4) can be written in terms of ΔE_d and ΔE_k, respectively as:

$$\mathrm{Log}\,(\Delta E_d(t_F)) = \mathrm{Log}\,\chi + c_{Ed}\,\mathrm{Log}A(t_F), \tag{33}$$

$$\mathrm{Log}\,(\Delta E_k(t_F)) = \mathrm{Log}\,\lambda + c_{Ek}\,\mathrm{Log}A(t_F), \tag{34}$$

where χ and λ are two coefficients, and c_{Ed} and c_{Ek} are estimates of the c coefficient in Richter laws (3) and (4).

In a similar way, we propose Eq. (8), which links the number of events $N(\geqslant E_r)$ to the released energy E_r, using the increments in ΔE_d and ΔE_k as:

$$\mathrm{Log}N(\geqslant \Delta E_d(t_F)) = \mathrm{Log}\,\theta + d_{Ed}\,\mathrm{Log}\,\Delta E_d(t_F), \tag{35}$$

$$\mathrm{Log}N(\geqslant \Delta E_k(t_F)) = \mathrm{Log}\,\tau + d_{Ek}\,\mathrm{Log}\,\Delta E_k(t_F), \tag{36}$$

where θ and τ are two additional coefficients, and d_{Ed}, d_{Ek} are estimates of the d coefficient in Eq. (8).

The values of ΔE_d and ΔE_k computed using Eqs. (30) and (31), in a certain interval of the simulation process, are plotted in Fig. 12a and b. The elastic (or potential), kinetic and dissipated energies are also illustrated in these diagrams. Time t_F indicates the instant at which the typical drop in the potential energy occurred during the simulation process.

A typical AE event is overlapped with the ΔE_d and ΔE_k increments during the simulation process in Fig. 13a. A zoom of the beginning of the events is presented in Fig. 13b, where it is clearly shown that the AE signal undergoes a certain delay in time with respect to the ΔE_k and ΔE_d increments. This is due to the fact that, when a localized fracture occurs in the specimen, the energy values are immediately computed, while the mechanical waves, which spread due to localized fracture in the specimen, need some additional time to arrive at the AE sensor.

Finally, the cumulative distributions of Eqs. (35) and (36), represented in the bi-logarithmic scale, are shown in Fig. 14. The d, b and c coefficients computed by means of the numerical simulation are summarized in Table 2.

Observing Table 2, it is possible to notice:

(i) The ratios b/d_{Ed} and b/d_{Ek} are close to the theoretical interval [1.5,2] indicated in the fundamental relations, Eqs. (3) and (6), presented in Section 3.
(ii) From the evaluation of the released energy, E_r, and the increments ΔE_d, ΔE_k, the d_{Ed} and d_{Ek} values also appear sensitive to the damage evolution, therefore the d-values decrease when damage and crack localization increase.
(iii) The (b/d_{Ek}) ratio near 1.5 indicates a better correlation with the fundamental relation presented in Eq. (6), and discussed in Section 3, than the (b/d_{Ed}) ratio. We should recall that Eq. (6) proposes a relationship between AE transient waves and released energy, which is related to the kinetic energy. Moreover, the good correlation between the typical AE events and the ΔE_k kinetic energy, shown in Fig. 13a, strengthens this observation.

10.4. AE frequency variations

Finally, we analyze the simulation results in terms of AE signal frequency variations. In Schiavi et al. [20], in which an experimental test similar to that analyzed in the present work was considered, the AE frequency variation was proposed as a parameter to evaluate the damage process. The results obtained in the present numerical simulation are given in Fig. 15.

Some remarks on the results in Fig. 15a and b are here presented:

(i) The highest peak frequencies (see (VII) in Fig. 15b) are related to the discretization level. If the elemental cube side is $L = 6$ mm, the Young's modulus $E = 9$ GPa, and the density $\rho = 2500$ kg/m^3, and if E and ρ are substituted in the expression of the p-wave velocity, $c_\rho = (E/\rho)^{0.5}$, we obtain $c_\rho = 1897$ m/s. On the other hand, the natural frequency of vibration related to the longitudinal bars is $f_c = 1/T_c$, where $T_c = 2 \times L/c_\rho$. Substituting the numerical values, we obtain $f_c = 160$ kHz, and in Fig. 15b a peak clearly appears close to f_c in both spectra.

(ii) The signal spectrum of two events is given in Fig. 15b. The first one has been selected at the beginning of the process ($t/t_{max} = 0.08$), the second, at the end ($t/t_{max} = 1$). It is possible to appreciate that the energy spectrum at the beginning of the process is concentrated close to a frequency of 70 kHz, while it shifts to 120 kHz at the end. Moreover, the signal energies are more distributed in the final stage of the damage process. The same trend has been found in Schiavi et al. [20].

(iii) The evolution of the two lower peak frequencies is presented in Fig. 15a. These frequencies are indicated with small circles in the two spectra and are marked with labels (I), (II) and (IV), (V) in Fig. 15a and b. The trend of these peaks to decrease when the damage process increases has also been observed by Schiavi et al. [20].

(iv) The evolution of the peak frequencies is shown in Fig. 15c and marked with labels (III) and (VI) in Fig. 15b. The values of the peak frequencies do not change significantly during the damage process. Only at the moment of the collapse their values change abruptly.

11. Conclusions

The statistical analysis of Acoustic Emission (AE) signals that emerge from growing microcracks is an effective damage assessment criterion for compression tests on concrete specimens. The signal amplitudes are distributed according to the Gutenberg–Richter (GR) law, and can be characterized through the b-value, which decreases systematically as the damage increases. An experimental compression test on a pre-damaged concrete specimen has been simulated using a version of the truss-like discrete element model (DEM). The experimental and numerical results have been analyzed considering the load vs. time diagram, and the b-value evolution obtained from AE events. The relationship between the AE data and energy parameters has also been addressed. Finally, the numerical results have been shown in terms of signal frequency variations during the damage process.

From these analyses, it is possible to draw the following conclusions.

(1) The comparison between the experimental and numerical results presents reasonable correlations, taking into account the particular way in which the test was carried out: the specimen was subjected to a pre-damage process before the main experimental test.

(2) Despite the difficulties in the numerical simulation, the obtained numerical b-values present values that are similar to the experimental ones, and in agreement with damage theories [15], showing a trend of b to decrease during the damage process.

(3) The correlations between the b-values, using the AE data, and the measurement of the released energy in terms of ΔE_d and ΔE_k increments, calculated by means of the numerical model, are in according to fundamental law proposed by Ritcher [18] and to the classical expression presented in Eq. (5). On the basis of this evaluation, it is interesting to note that the numerical d_{Ed} and d_{Ek} values also appear sensitive to the damage evolution, and that they decrease when damage and crack localization increase.

(4) The numerical results concerning the AE signal frequencies show variations that are consistent with the experimental results obtained by Schiavi et al. [20] on similar specimens.

(5) This study shows the potential applications of the truss-like Discrete Element Method (DEM) to simulate AE monitoring, and allows us to consider some possible future applications. Among others, it will be possible to simulate examples with other kind of boundaries condition, and problems with more complex geometries.

(6) The comparison between the experimental and numerical results also shown some aspects that must be improved in the model calibration, if we also reproduce the experimental results in terms of Acoustic Emission events.

Acknowledgements

The financial support provided by the *Regione Piemonte* (Italy) through the RE-FRESCOS Project is gratefully acknowledged. The authors wish also to thank the National Council for Scientific and Technological Development (CNPq, a Brazilian agency of financial aid) for funding this research.

References

[1] Lemaitre J, Chaboche JL. Mechanics of solid materials. Cambridge: University Press; 1990.
[2] Krajcinovic D. Damage mechanics. Amsterdam: Elsevier; 1996.
[3] Turcotte DL, Newman WI, Shcherbakov R. Micro and macroscopic models of rock fracture. Geophys J Int 2003;152:718–28.
[4] Shiotani T, Fujii K, Aoki T, Amou K. Evaluation of progressive failure using AE sources and improved b-value on slope model tests. Prog Acoust Emission 1994;7:529–34.

[5] Ohtsu M. The history and development of acoustic emission in concrete engineering. Mag Concr Res 1996;48:321–30.
[6] Colombo S, Main IG, Forde MC. Assessing damage of reinforced concrete beam using "*b*-value analysis of acoustic emission signals". ASCE J Mater Civil Engng 2003;15:280–6.
[7] Rao MVMS, Lakshmi KJP. Analysis of *b*-value and improved *b*-value of acoustic emissions accompanying rock fracture. Curr Sci 2005;89:1577–82.
[8] Kurz JH, Finck F, Grosse CU, Reinhardt HW. Stress drop and stress redistribution in concrete quantified over time by the *b*-value analysis. Struct Health Monit 2006;5:69–81.
[9] Carpinteri A, Lacidogna G, Niccolini G. Critical behaviour in concrete structures and damage localization by acoustic emission. Key Engng Mater 2006;312:305–10.
[10] Carpinteri A, Lacidogna G, Niccolini G, Puzzi S. Critical defect size distributions in concrete structures detected by the acoustic emission technique. Meccanica 2008;43:349–63.
[11] Lu C, Mai YW, Xie H. A sudden drop of fractal dimension: a likely precursor of catastrophic failure in disordered media. Philos Mag Lett 2005;85:33–40.
[12] Carpinteri A, Lacidogna G, Niccolini G, Puzzi S. Morphological fractal dimension versus power-law exponent in the scaling of damaged media. Int J Damage Mech 2009;18:259–82.
[13] Pollock AA. Acoustic emission-2: acoustic emission amplitudes. Non-Destruct Test 1973;6:264–9.
[14] Carpinteri A, Lacidogna G, Niccolini G. Fractal analysis of damage detected in concrete structural elements under loading. Chaos Soliton Fract 2009;42:2047–56.
[15] Carpinteri A, Lacidogna G, Puzzi S. From criticality to final collapse: evolution of the *b*-value from 1.5 to 1.0. Chaos Soliton Fract 2009;41:843–53.
[16] Carpinteri A. Scaling laws and renormalization groups for strength and toughness of disordered materials. Int J Solid Struct 1994;31:291–302.
[17] Rundle J, Turcotte D, Shcherbakov R, Klein W, Sammis C. Statistical physics approach to understanding the multiscale dynamics of earthquake fault systems. Rev Geophys 2003;4. 8755–1209.
[18] Richter CF. Elementary seismology. San Francisco and London: W.H. Freeman; 1958.
[19] Scholz CH. The frequency–magnitude relation of microfracturing in rock and its relation to earthquakes. Bull Seism Soc Am 1968;58:99–415.
[20] Schiavi A, Nicolini G, Tarizzo P, Carpinteri A, Lacidogna G, Manuello A. Acoustic emissions at high and low frequencies during compression tests in brittle materials. Strain 2011;47(Suppl. 2):105–10.
[21] Kanamori H, Anderson DL. Theoretical basis of some empirical relations in seismology. Bull Seismol Soc Am 1975;5:1073–95.
[22] Carpinteri A, Lacidogna G, Pugno N. Structural damage diagnosis and life-time assessment by acoustic emission monitoring. Engng Fract Mech 2007;74:273–89.
[23] Chakrabarti BK, Benguigui LG. Statistical physics of fracture and breakdown in disordered systems. Oxford: Clarendon Press; 1997.
[24] Nayfeh AH, Hefzy MS. Continuum modeling of three-dimensional truss-like space structures. AIAA J 1978;8:779–87.
[25] Dalguer LA, Irikura K, Riera JD, Chiu HC. The importance of the dynamic source effects on strong ground motion during the 1999 Chi-Chi, Taiwan, earthquake: brief interpretation of the damage distribution on buildings. Bull Seismol Soc Am 2001;91:1112–27.
[26] Dalguer LA, Irikura K, Riera JD. Simulation of tensile crack generation by three-dimensional dynamic shear rupture propagation during an earthquake. J Geophys Res 2003;108(B3):2144.
[27] Riera JD. Local effects in impact problems on concrete structures. In: Proceedings, conference on structural analysis and design of nuclear power plants, vol. 3, CDU, Porto Alegre, RS, Brasil; 1984 [264.04:621.311.2:621.039].
[28] Rios RD, Riera JD. Size effects in the analysis of reinforced concrete structures. Engng Struct 2004;26:1115–25.
[29] Hillerborg A. A model for fracture analysis. Cod LUTVDG/TVBM 1976;300:51–81.
[30] Rocha MM, Riera JD, Krutzik NJ. Extension of a model that aptly describes fracture of plain concrete to the impact analysis of reinforced concrete. In: Int conf and structural mechanics in reactor technology, SMiRT 11, Trans vol. J, Tokyo, Japan; 1991.
[31] Riera JD, Rocha MM. A note on the velocity of crack propagation in tensile fracture. Revista Brasileira de Ciencias Mecanicas 1991;3:217–40.
[32] Miguel LFF, Riera JD, Kaminski Jr. J, Fadel MLF, Menezes RCR. Model uncertainty in the definition of EPS wind loads in transmission line design. In: ICWE 12 – twelfth international conference on wind engineering, Cairns, vol. 2; 2007. p. 1567–74.
[33] Riera JD, Iturrioz I. Discrete element dynamic response of elastoplastic shells subjected to impulsive loading. Commun Numer Meth Engng 1995;11:417–26.
[34] Riera JD, Iturrioz I. Discrete element model for evaluating impact and impulsive response of reinforced concrete plates and shells subjected to impulsive loading. Nucl Engng Des 1998;179:135–44.
[35] Schnaid F, Spinelli L, Iturrioz I, Rocha M. Fracture mechanics in ground improvement design. Ground Improv 2004;8:7–15.
[36] Miguel LFF, Riera JD, Iturrioz I. Influence of size on the constitutive equations of concrete or rock dowels. Int J Numer Anal Meth Geomech 2008;32. 1857–81.
[37] Iturrioz I, Miguel LFF, Riera JD. Dynamic fracture analysis of concrete or rock plates by means of the discrete element method. Lat Am J Solids Struct 2009;6:229–45.
[38] Kosteski L, Barrios R, Iturrioz I. Fractomechanics parameter calculus using the discrete element method. Lat Am J Solids Struct 2009;6:301–21.
[39] Kosteski L, Iturrioz I, Batista RG, Cisilino AP. The truss-like discrete element method in fracture and damage mechanics. Engng Comput 2011;6:765–87.
[40] Kosteski LE, Barrios R, Iturrioz I. Crack propagation in elastic solids using the truss-like discrete element method. Int J Fract 2012. http://dx.doi.org/10.1007/s10704-012-9684-4.
[41] Riera JD, Miguel LFF, Iturrioz I. Strength of brittle materials under high strain rates in DEM simulations. Comput Model Engng Sci 2011;82(2):113–36.
[42] Krajcinovic D, Vujosevic M. Strain localization – short to long correlation length transition. Int Solids Struct 1998;35(31–32):4147–66.
[43] Sagar RV, Raghu Prasad BK. Modeling heterogeneity of concrete using 2D lattice network for concrete fracture and comparison with AE study. Sadhana 2009;34, part 6(12):865–86.
[44] Nagy E, Landis EN, Davids WG. Acoustic emission measurements and lattice simulations of microfracture events in spruce. Holzforschung 2010;64:455–61. http://dx.doi.org/10.1515/HF.2010.088.